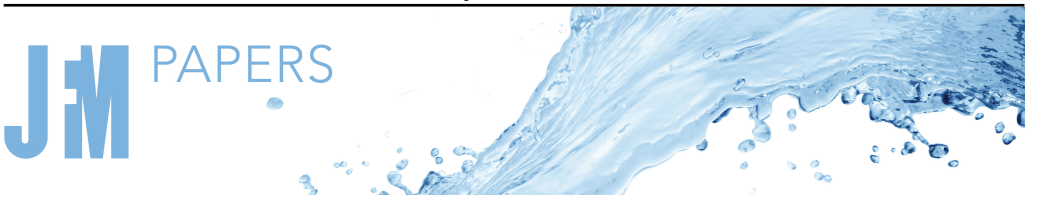
J. Fluid Mech. (2026), *vol.* 1028, A17, doi:10.1017/jfm.2025.11108



Unified scaling laws in porous-medium vertical natural convection

Feixiong Rao[1] **and Shengqi Zhang**[2]

[1]College of Engineering, Zhejiang Normal University, Jinhua, Zhejiang 321004, PR China

[2]Ningbo Key Laboratory of Advanced Manufacturing Simulation, Eastern Institute of Technology, Ningbo, Zhejiang 315201, PR China

Corresponding author: Shengqi Zhang, szhang@eitech.edu.cn

(Received 9 September 2025; revised 19 December 2025; accepted 20 December 2025)

This study conducted theoretical analysis and direct numerical simulations (DNS) of vertical natural convection in a two-dimensional cavity filled with porous media, where the imposed temperature gradient is oriented perpendicular to the direction of gravity. Three regimes characterised by distinct flow states and the angle θ of the isothermal layer are identified. In the steady regime I with $\theta \approx \pi/2$, the flow is weak and heat transfer is dominated by conduction. In the transitional regime II with rapidly increasing θ, kinetic and thermal boundary layers gradually develop. In the turbulent regime III with $\theta \approx 0$, clear boundary layers arise and turbulent thermal convection prevails. Corresponding to these flow states, theoretical analysis is performed to derive the scaling laws of the Nusselt number $Nu - 1 \sim Ra_D^{\gamma_1} Pr^{\eta_1}$ and Reynolds number $Re \sim Ra_D^{\gamma_2} Pr^{\eta_2}$ with respect to Rayleigh–Darcy number Ra_D and Prandtl number Pr. We derive $(\gamma_1, \gamma_2, \eta_1, \eta_2) = (2, 1, 0, -1)$ for the steady regime and $(1/3, 4/9, 0, -2/3)$ for the turbulent regime. All theoretical scaling exponents in these two regimes are validated by DNS results. Furthermore, we find that the influence of the Darcy number Da becomes almost negligible when it is sufficiently small. Unified models for $Pr = 1$ are proposed to integrate the three regimes and are applicable across a broad range of ϕ and Ra_D, which are satisfactorily verified by DNS results. The unified models provide a predictive framework for heat transport and flow intensity in porous-medium thermal convection, thereby offering practical values for thermal engineering applications.

Key words: convection in porous media, turbulence theory, turbulence simulation

1. Introduction

Thermally driven convective fluid motions represent a fundamental process widely observed in both geophysical and astrophysical systems, and they are essential for

© The Author(s), 2026. Published by Cambridge University Press.

https://doi.org/10.1017/jfm.2025.11108 Published online by Cambridge University Press

numerous industrial applications. Classical models, such as Rayleigh–Bénard convection (RBC) (Bodenschatz, Pesch & Ahlers 2000; Ahlers, Grossmann & Lohse 2009; Zhang *et al.* 2020; Ecke & Shishkina 2023; Lohse & Shishkina 2024) and vertical natural convection (Ng *et al.* 2015; Shishkina 2016), have been extensively studied to uncover the fundamental mechanisms governing heat and momentum transport. In RBC, the fluid is heated from below and cooled from above, while in vertical natural convection, the fluid is confined between two vertical walls with differing temperatures. These models provide critical insights into the dynamics of buoyancy-driven flows and their roles in large-scale environmental and engineering systems.

Vertical natural convection holds significant practical importance, with applications ranging from thermal insulation in double-pane windows and horizontal heat transport in water reservoirs to crystal growth processes and the cooling of electronic devices. Furthermore, it serves as an idealised model for studying thermally driven atmospheric and oceanic circulations, providing a framework for understanding large-scale environmental flow phenomena (Lappa 2009). Despite extensive research being devoted to vertical natural convection, questions remain regarding the evolution of flow and heat transfer as the Rayleigh number Ra increases across various flow regimes.

A key research question in vertical natural convection is the scaling exponents of Nusselt number $Nu \sim Ra^{\gamma_1}$ and Reynolds number $Re \sim Ra^{\gamma_2}$. Research studies conducted by Trias *et al.* (2007, 2010), Ng *et al.* (2015, 2020), Shishkina (2016) and Wang *et al.* (2019, 2021) report that the scaling exponent γ_1 varies between 1/4 and 1/3, while γ_2 varies between 1/2 and 4/9, depending on the specific ranges of Ra and Prandtl number Pr. For $Pr \gg 1$, Shishkina (2016) applied laminar boundary layer theory to theoretically derive the scaling exponents $\gamma_1 = 1/4$ and $\gamma_2 = 1/2$. These findings were corroborated by Ng *et al.* (2020) through direct numerical simulations (DNS) of three-dimensional vertical convection with periodic boundary conditions. Consequently, within the small range of Ra, γ_1 tends to approximate to 1/4 (Trias *et al.* 2007, 2010; Wang *et al.* 2019). However, as Ra increases, γ_1 approaches approximately 0.31 (Ng *et al.* 2015). In the larger range of Ra, γ_1 is approximately 1/3, while γ_2 is approximately 4/9 (Wang *et al.* 2021), which aligns with the results of RBC and is consistent with Grossman–Lohse (GL) theory (Grossmann & Lohse 2000; Lohse & Xia 2010).

Compared with the pure thermal convection in the above studies, porous-medium thermal convection is receiving increased attention. Investigating thermal convection in porous media is essential due to its wide-ranging applications in engineering and environmental systems (Nield & Bejan 2006; Rebhi *et al.* 2022), including the design of heat exchangers, geothermal energy extraction and cooling systems for electronic devices (Odenthal *et al.* 2014). Pore-scale turbulent convection enhances heat transfer by actively driving fluid through the porous structure, thereby optimising thermal performance in systems where heat transfer alone is insufficient. As industries increasingly demand higher energy efficiency and precision, the investigation of porous-medium thermal convection becomes imperative for effective heat management.

The scaling laws of porous-medium thermal convection represent a fundamental area of research. Currently, two primary methods are employed to investigate this question: DNS (Liu *et al.* 2020, 2021; Li, Yang & Sun 2024) and macroscopic models (Pirozzoli *et al.* 2021; De Paoli 2023; Hu & Yang 2024; Zhu, Fu & De Paoli 2024). However, the existing studies predominantly focus on porous-medium RBC. The mechanisms underlying porous-medium vertical natural convection, especially with pore-scale turbulence, remain inadequately understood. Consequently, this study aims to address the following primary questions: (i) What are the major regimes of porous-medium vertical natural convection? (ii) What are the scaling laws of Nu and Re? (iii) Are there unified scaling models for

https://doi.org/10.1017/jfm.2025.11108 Published online by Cambridge University Press

$Nu(Ra_D, \phi, Da)$ and $Re(Ra_D, \phi, Da)$? Here, Ra_D, ϕ and Da refer to the Rayleigh–Darcy number, porosity and Darcy number, respectively.

This study employs theoretical analysis and DNS to investigate porous-medium vertical natural convection across a wide range of Ra_D, ϕ and Da. We identify three distinct regimes based on the characteristics of the flow states. Subsequently, we theoretically derive scaling laws for Nu and Re within each regime. Furthermore, we propose unified scaling models at $Pr = 1$. The models are validated by DNS results across a broad spectrum of (Ra_D, ϕ, Da). Through this study, we aim to enhance the understanding of regime transitions and the development of unified scaling laws in porous-medium vertical natural convection.

This paper is organised as follows: § 2 discusses the governing equations, the geometry set-ups and the numerical methods employed. In § 3, we present the corresponding simulation results and engage in a discussion of these findings. The posed questions are comprehensively addressed. Finally, § 4 presents the conclusions drawn from this study.

2. Governing equations, basic set-ups and numerical methods

2.1. *Governing equations*

The governing equations for DNS consist of the incompressible Navier–Stokes equations and the thermal transport equation, as presented in (2.1*a*–*c*)

$$\partial u_i/\partial x_i = 0, \tag{2.1a}$$

$$\partial u_i/\partial t + \partial\left(u_i u_j\right)/\partial x_j = -\rho^{-1}\partial p/\partial x_i + \nu\partial^2 u_i/\partial x_j^2 - g_i\beta(T - T_0), \tag{2.1b}$$

$$\partial T/\partial t + \partial(u_i T)/\partial x_i = \alpha\partial^2 T/\partial x_i^2. \tag{2.1c}$$

Here, u_i is the velocity, p is the pressure, T is the temperature with reference value T_0, β is the thermal expansion coefficient, g_i is the applied gravitational acceleration, ν is the kinematic viscosity and α is the thermal diffusivity. The Oberbeck–Boussinesq approximation, assuming variations in density $\rho \approx \rho_0[1 - \beta(T - T_0)]$, are negligible except in the buoyancy term, is adopted.

2.2. *The set-ups of geometry and important parameters*

As illustrated in figure 1, the two-dimensional square cavity with size H is filled with a porous medium. The porous medium consists of a $N_r \times N_r$ array of representative elementary volumes (REVs) with size $S = H/N_r$, which accurately captures the pore-scale properties of the entire domain. Each REV features a solid square element with size d at its centre, which adheres to no-slip and adiabatic (i.e. impermeable in the context of solutal convection) boundary conditions, resulting in porosity $\phi = 1 - (d/S)^2$. The gravitational acceleration $\boldsymbol{g} = (0, -g, 0)$ acts downward, directing the buoyancy forces of the hot fluid upwards. The thermal boundary conditions for the top and bottom walls are adiabatic, while the left and right walls are maintained at constant temperatures of $T_0 + \Delta/2$ and $T_0 - \Delta/2$, respectively.

In relation to the porous medium within the cavity, the Darcy number is defined as

$$Da = K/H^2, \tag{2.2}$$

where K represents permeability, quantifying the ability of the porous medium to facilitate fluid flow. Permeability is determined using Darcy's law $K = u_{Di}\nu/g_i$, where u_{Di} is the volume-averaged velocity in a REV for Stokes flow (Rao & Zhang 2025*c*). It is important

https://doi.org/10.1017/jfm.2025.11108 Published online by Cambridge University Press

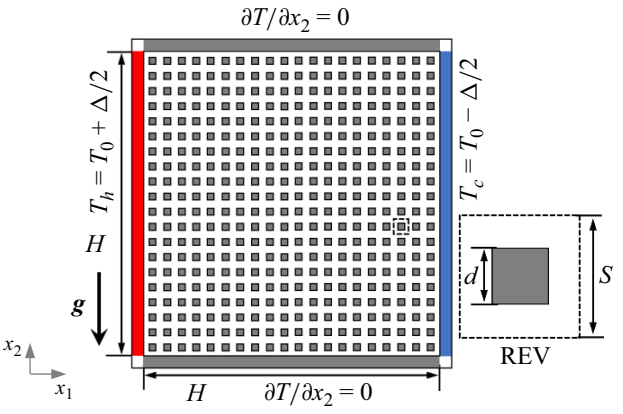


Figure 1. The schematic geometry and set-ups employed in DNS.

to note that K is calculated directly through DNS rather than relying on empirical equations, thus enhancing its accuracy. Regarding the presence of porous medium, the Rayleigh–Darcy number Ra_D is employed instead of the conventional Rayleigh number $Ra = g\beta\Delta H^3/(\nu\alpha)$ and is defined as

$$Ra_D = Ra \cdot Da. \tag{2.3}$$

The Nusselt number is defined as the ratio of total heat transfer to static conductive heat transfer at the conducting boundary in the fluid, and is expressed as follows:

$$Nu = (\langle \partial_1 T \rangle_A / \langle \partial_1 T_{Ra=0} \rangle_A)\,|_{x_1=\pm H/2}, \tag{2.4}$$

where $\langle \cdot \rangle_A|_{x_1=\pm H/2}$ represents the time- and area-averaged value at position $x_1 = \pm H/2$. The global Reynolds number is defined as

$$Re = U_D H/\nu, \tag{2.5}$$

where the root-mean-square velocity $U_D = \phi U$ and $U = \sqrt{\langle u_i u_i \rangle_f}$. Here, $\langle \cdot \rangle_f$ denotes the time- and intrinsic volume-averaged value for the fluid phase. The Prandtl number $Pr = \nu/\alpha$ is defined as the ratio of momentum diffusivity (viscosity) to thermal diffusivity. In this study, we mainly focus on the scaling laws with respect to Ra_D, ϕ and Da. Therefore, we fix the Prandtl number at 1 for most simulation cases.

2.3. *Numerical methods*

In this study, the finite volume method (FVM) and lattice Boltzmann method (LBM) are employed for simulations. The solver pimpleFoam, based on OpenFOAM, has been modified to effectively couple the flow and temperature dynamics. A second-order central difference scheme is utilised for the spatial discretisation of both velocity and temperature, achieved through the interpolation of variables at the interfaces of grid cells. The Poisson equation is solved at each time step to update the pressure, while the pressure-implicit with splitting of operators scheme ensures accurate coupling between pressure and velocity. The LBM is employed to indirectly solve microscopic equations by determining particle distributions. The fundamental equation in LBM is a discretised version of the Boltzmann equation, with the collision operator addressed by the Bhatnagar–Gross–Krook model. Both the FVM and LBM solvers have undergone rigorous validation and verification in prior research (Rao, Kuznetsov & Jin 2020; Rao 2022; Rao & Jin 2022; Rao & Zhang 2025*a*,*b*,*c*); therefore, they are directly utilised in this study. All cases are calculated

https://doi.org/10.1017/jfm.2025.11108 Published online by Cambridge University Press

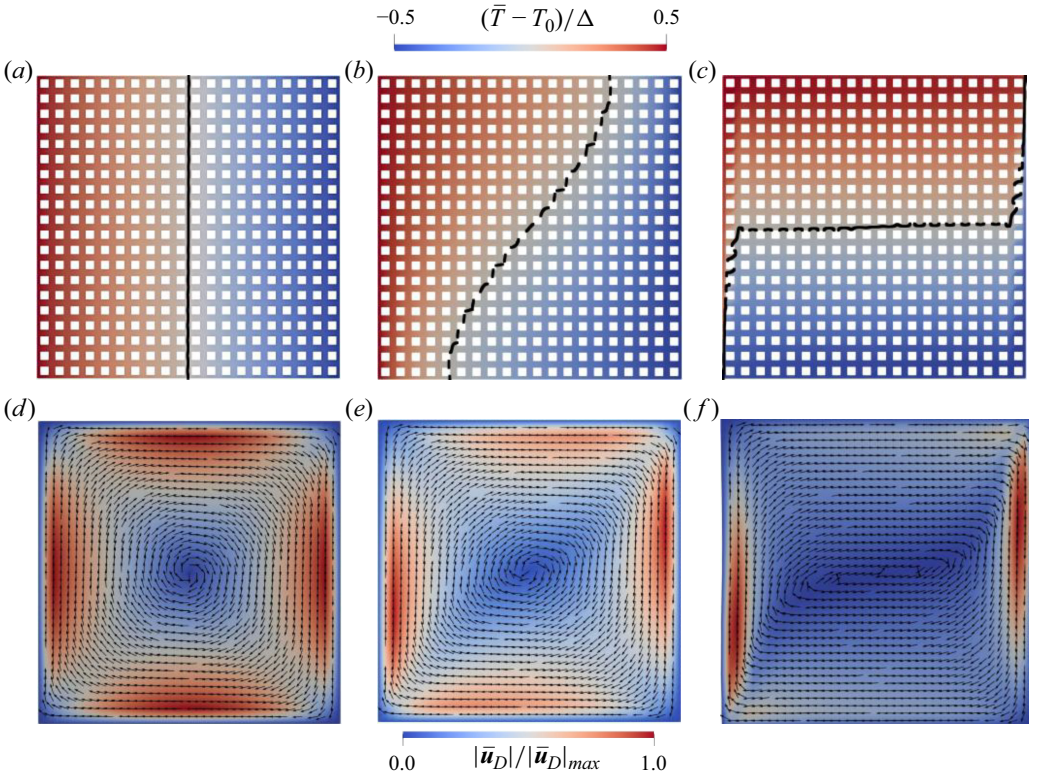


Figure 2. (*a*,*b*,*c*) Time-averaged temperature $\overline{T}$ contour with isothermal layer $\overline{T} = T_0$ and (*d*,*e*,*f*) filtered time- and REV-averaged velocity vectors and magnitude contour in three regimes at $\phi = 0.69$, $Da = 2.1 \times 10^{-5}$. Panels show (*a*,*d*) $Ra_D = 2.1 \times 10^{-2}$; (*b*,*e*) $Ra_D = 4.2 \times 10^{1}$; (*c*,*f*) $Ra_D = 2.1 \times 10^{4}$.

using two distinct mesh resolutions, employing $(60S/d + 1)^3$ grid points for each REV for laminar flow and $(90S/d + 1)^3$ grid points for each REV for turbulent flow. This methodology aims to achieve a balance between mesh independence and computational cost. The computational duration is established at a minimum of 100 time periods $t = H/u_m$, where $u_m = g\beta\Delta K/\nu$ is the characteristic velocity. Furthermore, the calculated Nusselt number is consistent for the hot and cold plates.

3. Results and discussion

3.1. *Flow states*

To answer the questions raised in § 1, we conducted a series of DNS simulations across a range of Ra_D from 0 to 10^8. As illustrated in figure 2(*a–c*), which shows time-averaged temperature fields, our observations reveal three distinct regimes, characterised by the angle θ between the isothermal layer $\overline{T} = T_0$ and the x_1 axis. It is important to note that these three regimes pertain specifically to the bulk region. For clarity, in figure 2(*d–f*) we depict the velocity vectors and amplitude contours by mapping the time- and REV-averaged velocity $\overline{u}_{Di}$ onto a pure cavity of identical dimensions. Here, $\overline{\cdot}$ denotes the time average.

Regime I (steady regime, distinct vertical isothermal layer): heat transfer is predominantly governed by conduction. The flow is characterised by a steady state with a small velocity amplitude, which allows for the applicability of the Stokes approximation in the momentum equation. The viscous term nearly balances the buoyancy term, resulting

https://doi.org/10.1017/jfm.2025.11108 Published online by Cambridge University Press

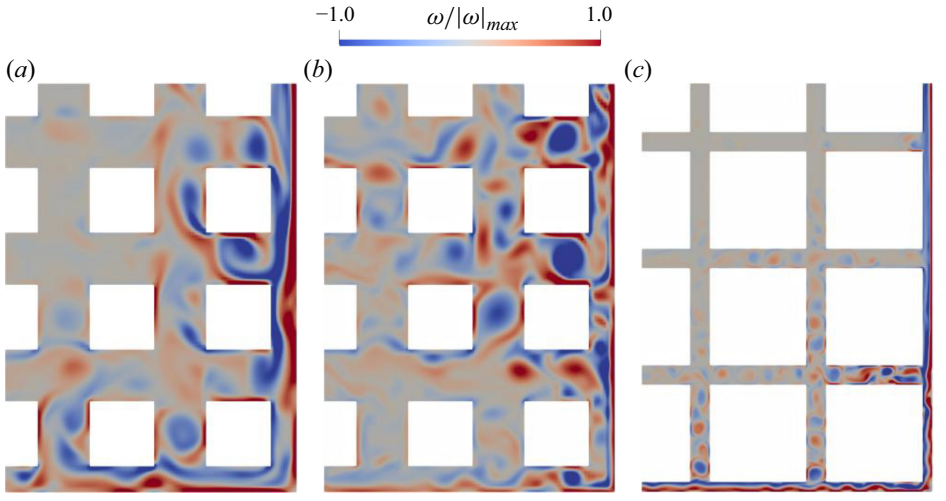


Figure 3. The zoom-in snapshots of instantaneous turbulent structures near the bottom-right corner in the turbulent regime. Panels show (*a*) $Ra_D = 2.1 \times 10^4$, $\phi = 0.69$; (*b*) $Ra_D = 1.0 \times 10^8$, $\phi = 0.69$; (*c*) $Ra_D = 1.0 \times 10^8$, $\phi = 0.31$.

in a weak circulation around the cavity, as illustrated in figure 2(*d*). In this regime, the temperature distribution is almost linear across the REVs. Subsequently, a large-scale convection cell is established, which resembles porous-medium RBC. Although both velocity and heat transfer are expected to increase with Ra_D, their impact on the distribution of temperature is minimal, leading to distinct vertical isothermal layer where $T \approx T_{Ra_D=0}$, $Nu \approx 1$ and $\theta \approx \pi/2$.

Regime II (transitional regime, distinct mixed isothermal layer): heat transfer is primarily governed by both thermal conduction and convection, allowing $Nu - 1$ to reach the scale of $O(1)$. Figure 2(*e*) suggests that $|\overline{\boldsymbol{u}}_D|$ begins to concentrate in elongated vertical regions near the sidewalls, indicating the formation of kinetic and thermal boundary layers. Similar to porous-medium RBC, the large-scale structure in the flow field begins to exhibit disorder. Consequently, thermal convective instability gradually develops near the hot and cold walls, impacting heat transfer. Furthermore, as illustrated in figure 2(*b*), the isothermal layer deviates from the x_2 axis towards the x_1 axis, signifying a distinct mixed isothermal layer with $0 < \theta < \pi/2$.

Regime III (turbulent regime, distinct horizontal isothermal layer): heat transfer is predominantly governed by a weak and pore-scale turbulent flow (Rao *et al.* 2020; Rao & Jin 2022; Rao & Zhang 2025*a*,*b*,*c*). The onset of turbulence in this regime induces spatio-temporal chaos: the flow originating from the bottom near the left wall rises directly to the top, while the flow originating from the top near the right wall descends to the bottom, as illustrated in figure 2(*c*,*f*). The vorticity, defined as $\omega = \partial u_2/\partial x_1 - \partial u_1/\partial x_2$, is utilised to qualitatively identify turbulent structures within porous media, as it effectively captures vortex structures of varying strengths, as illustrated in figure 3. The results indicate that an increase in Ra_D correlates with an intensified vorticity strength, while a decrease in ϕ is associated with a reduction in the high-vorticity region. Turbulence is primarily concentrated near the sidewalls, resulting in a significant increase in the Nusselt number. The temperature distribution leads to the formation of a distinct horizontal isothermal layer with $\theta \approx 0$.

Furthermore, we apply two statistical methods to identify the three regimes. Method 1 involves calculating the volume-averaged temperature within each REV and subsequently

https://doi.org/10.1017/jfm.2025.11108 Published online by Cambridge University Press

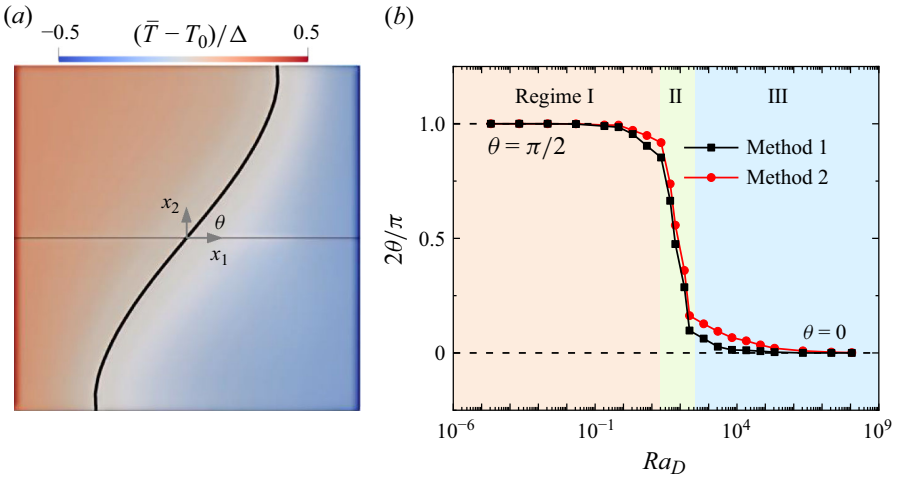


Figure 4. (*a*) Filtered time- and REV-averaged temperature contour with isothermal layer $\overline{T}=T_0$. (*b*) The profile of θ-Ra_D at $\phi=0.69$, $Da=2.1\times10^{-5}$.

mapping all REV-averaged values to a pure cavity of identical size. The angle $\theta=\arctan(\Delta x_2/\Delta x_1)$ between the isothermal layer and the x_1 axis is then calculated, as illustrated in figure 4(*a*). Method 2 employs $\theta=\pi/2\ -\arctan(\langle T\cdot x_2\rangle_f/\langle T\cdot x_1\rangle_f)$ to determine the corresponding angle. Figure 4(*b*) shows the profile of $\theta-Ra_D$ across three distinct regimes. In both regimes I and III, θ increases slowly with values close to $\pi/2$ and 0, respectively. In the transitional regime II, θ increases dramatically over a small range of Ra_D, showing that convection begins to significantly influence the temperature distribution. In addition, the profile of $\theta-Ra_D$ is almost rotationally symmetric about the point at the centre of regime II and $\theta=\pi/4$. The angle obtained by method 2 is larger than that obtained by method 1, particularly in regime II, as method 2 incorporates the thermal distribution across the entire area, while method 1 only accounts for the thermal distribution in the central region.

3.2. *Scaling laws of Nu and Re*

This section aims to theoretically derive unified scaling laws for *Nu* and *Re* in porous-medium vertical natural convection. This analysis encompasses a broad spectrum of input parameters (Ra_D, ϕ, Da, Pr), as these parameters are crucial for facilitating rapid predictions of heat transfer efficiency and flow intensity. To ensure a smooth derivation, two coarse-grained physical coefficients, the permeability K and static effective diffusivity $\tilde{\alpha}_0$, must be determined in advance. Here, $\tilde{\alpha}_0$ is defined by the cavity-scale extension of Fourier's law. In this study, we focus solely on the channels within the porous matrix, as they primarily determine the values of permeability and static effective diffusivity. Based on the approximate analysis of Stokes flow and static conduction, these two terms can be expressed as follows:

$$K\approx H^2(1-\sqrt{1-\phi})^3/\left(12N_r^2\right), \tag{3.1a}$$

$$\tilde{\alpha}_0=-(\alpha\langle\partial_1 T_{Ra=0}\rangle_A|_{x_1=\pm H/2})H/\Delta\approx\alpha\left(1-\sqrt{1-\phi}\right). \tag{3.1b}$$

Regarding the presence of the porous matrix, the expressions for the global kinetic and thermal dissipation rates are adjusted, as shown below (see Appendix A)

https://doi.org/10.1017/jfm.2025.11108 Published online by Cambridge University Press

$$\varepsilon_u = \nu\langle \partial_i u_j \partial_i u_j \rangle_V = \beta g \langle u_2 T \rangle_V, \tag{3.2a}$$

$$\varepsilon_T = \alpha\langle \partial_i T \partial_i T \rangle_V = \tilde{\alpha}_0 \Delta^2 H^{-2} Nu = \tilde{\alpha}_0 \Delta^2 H^{-2} + \alpha\langle \partial_i \delta T \partial_i \delta T \rangle_V, \tag{3.2b}$$

where $\langle \cdot \rangle_V$ denotes the time- and whole volume-averaged value including the fluid and solid phases. Here, $\delta T = T - T_{Ra=0}$ and $T_{Ra=0}$ represents the temperature distribution when $Ra = 0$.

3.2.1. *Steady regime*

In this regime, the total drag caused by the porous matrix, as approximated by Darcy's law, equals the buoyancy term induced by the temperature difference and $T \approx T_{Ra=0}$. Consequently, it is straightforward to derive the scaling law of Re

$$\phi \nu K^{-1} u_{Di} \sim -\phi g_i \beta \left(T_{Ra=0} - T_0\right) \Rightarrow u_{Di} \sim g_i \beta \Delta K \nu^{-1} \Rightarrow Re \sim Ra_D Pr^{-1}. \tag{3.3}$$

This also indicates that the transitional regime, representing the onset of deviation from Stokes approximation, should be characterised by Ra_D and Pr.

Notably, $\partial_i^2 T_{Ra=0} = 0$ and $\partial_1 T_{Ra=0} \sim -\Delta H^{-1}(\tilde{\alpha}_0/\alpha)$ in this regime. Consequently, the scaling of δT can be derived based on steady macroscopic energy equation (Rao & Zhang 2025*a*,*b*)

$$\phi^{-1} u_{Di} \partial_i T_{D,Ra=0} = \tilde{\alpha}_0 \nabla^2 \delta T_D \Rightarrow \delta T \sim \phi^{-1} \Delta H \alpha^{-1} u_{Di} \sim \phi^{-1} Ra_D \Delta. \tag{3.4}$$

The scaling law for Nu is derived by combining (3.2*b*) and (3.4), as shown below

$$Nu - 1 = \left(\tilde{\alpha}_0 \Delta^2 H^{-2}\right)^{-1} \alpha \langle \partial_i \delta T \partial_i \delta T \rangle_V \sim Ra_D^2 \left(\phi\left(1 - \sqrt{1-\phi}\right)\right)^{-1}. \tag{3.5}$$

3.2.2. *Turbulent regime*

In this regime, the GL theory and the process of its derivation (Ahlers *et al.* 2009) are applied with adjustments concerning the porous matrix. The total heat flux can be further elaborated based on the definition of Nu

$$\tilde{\alpha}_0 \Delta H^{-1} Nu = -\alpha \langle \partial_1 T \rangle|_{x=\pm H/2} = \langle u_1 T - \alpha \partial_1 T \rangle_A \approx \langle u_1 T \rangle_V. \tag{3.6}$$

It can be inferred from figure 2(*c*,*f*) that $\langle u_1 T \rangle_V$ is dominated by the convective heat flux along the stratified regions near the horizontal walls, while $\langle u_2 T \rangle_V$ is dominated by the convective heat flux along the boundary layers near vertical walls. With the heat input/output from vertical walls, the vertical heat fluxes caused by u_2 gradually increases along their flow paths, and change directions at the top-left/bottom-right corner, transitioning to the heat flux primarily driven by $u_1 T$. Consequently, it is reasonable to estimate that

$$(u_1 T \delta x_2)_{\rightleftarrows} \approx 2 (u_2 T \delta x_1)_{\uparrow\downarrow} \Rightarrow \langle u_1 T \rangle_V \sim \langle u_2 T \rangle_V, \tag{3.7}$$

where $\rightleftarrows$ refers to the rightward/leftward flow near the upper/lower plate, and $\uparrow\downarrow$ refers to the upward/downward flow near the left/right plate. Therefore, by combining (3.2*a*), (3.6) and (3.7) we can get

$$\varepsilon_u \sim \beta g \tilde{\alpha}_0 \Delta H^{-1} Nu. \tag{3.8}$$

Considering the presence of porous matrix, the no-slip and adiabatic boundary conditions imposed on the porous matrix, $\langle \cdot \rangle_V = \phi \langle \cdot \rangle_f$, $\partial_i u_j \sim U/(S \times (1 - \sqrt{1-\phi})) = (U \times N_r)/(H \times (1 - \sqrt{1-\phi}))$, $\partial_i T \sim \Delta/(H \times (1 - \sqrt{1-\phi}))$. By integrating these with the original definitions of ε_u and ε_T in (3.2), the global kinetic and thermal dissipation rates are adjusted

https://doi.org/10.1017/jfm.2025.11108 Published online by Cambridge University Press

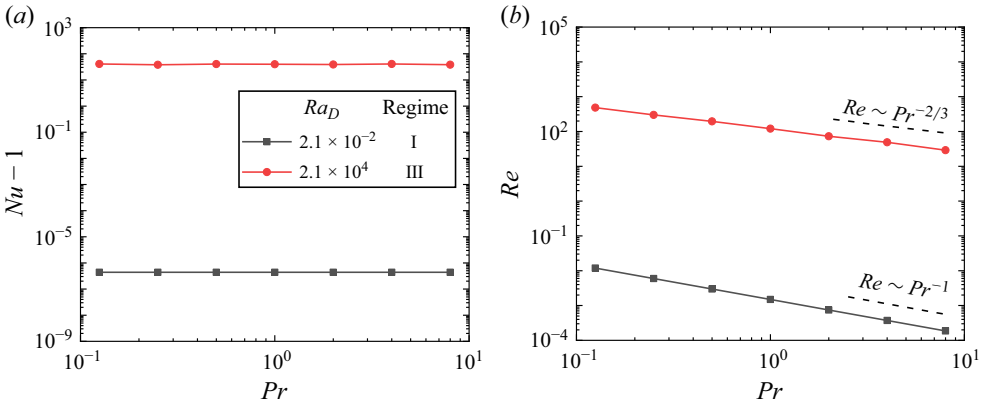


Figure 5. Validation of the scaling law exponents with respect to Pr. Here, $\phi = 0.69$, $Da = 2.1 \times 10^{-5}$. Panels show (*a*) $Nu - 1$; (*b*) Re. Panels (*a*) and (*b*) share the same legend.

$$\varepsilon_u \sim U^3 H^{-1} \times \phi \times (H/(S-d))^2 \sim U^3 H^{-1} N_r^2 \phi \left(1 - \sqrt{1-\phi}\right)^{-2}, \tag{3.9a}$$

$$\varepsilon_T \sim \Delta^2 H^{-1} U \lambda_T \lambda_u^{-1} \times \phi \times (S/(S-d))^2 \sim \Delta^2 H^{-1} U \lambda_T \lambda_u^{-1} \phi \left(1 - \sqrt{1-\phi}\right)^2, \tag{3.9b}$$

where $\lambda_u = HRe^{-1/2}$ and $\lambda_T = H(2\tilde{\alpha}_0 Nu/\alpha)^{-1}$. Combining (3.2*b*), (3.8) and (3.9), we can finally get

$$Nu \sim Ra_D^{1/3} \left(\phi\left(1 - \sqrt{1-\phi}\right)\right)^{-1} \left(\left(1 - \sqrt{1-\phi}\right)/\phi\right)^{-5/3}, \tag{3.10a}$$

$$Re \sim Ra_D^{4/9} Pr^{-2/3} \left(\left(1 - \sqrt{1-\phi}\right)/\phi\right)^{-8/9}. \tag{3.10b}$$

3.3. *Validation of scaling laws with respect to Pr*

In this subsection, we validate the scaling laws of Nu and Re with respect to Pr. Since the derived equations provide the scaling law exponents exclusively for the steady and turbulent regimes, as discussed in § 3.2, we concentrate our validation efforts on these two regimes. Consequently, we maintain fixed values of Ra_D and ϕ, which would be validated in § 3.4. The Prandtl number is defined as $Pr = 2^n$, where the integer n varies from -3 to 3. The DNS results are illustrated in figure 5. Our findings indicate that the Nusselt number exhibits approximate independence from the Prandtl number. In the steady regime, the calculated Nusselt number is distinctly identified. Conversely, in the turbulent regime, we observe slight fluctuations, which may be attributed to the size matching between pore-scale and turbulent structures. Furthermore, the results imply that the scaling law exponent for Re is -1 in the steady regime and $-2/3$ in the turbulent regime. The DNS results effectively validate the scaling laws of $Nu - 1$ and Re with respect to Pr derived from theoretical frameworks. It is important to note that this study exclusively considers Pr values within the range of [0.125, 8].

3.4. *Unified scaling models and validation for Pr = 1*

This subsection aims to establish unified scaling models for Nu and Re across the three regimes of porous-medium vertical natural convection. The development of these unified scaling models is crucial, as they enable the rapid determination of corresponding Nu and Re values based on prior Ra_D and ϕ, thereby benefiting industrial applications. In this study, Pr is set to 1, and for the range of porosity considered, $(1 - \sqrt{1-\phi})/\phi$ can

https://doi.org/10.1017/jfm.2025.11108 Published online by Cambridge University Press

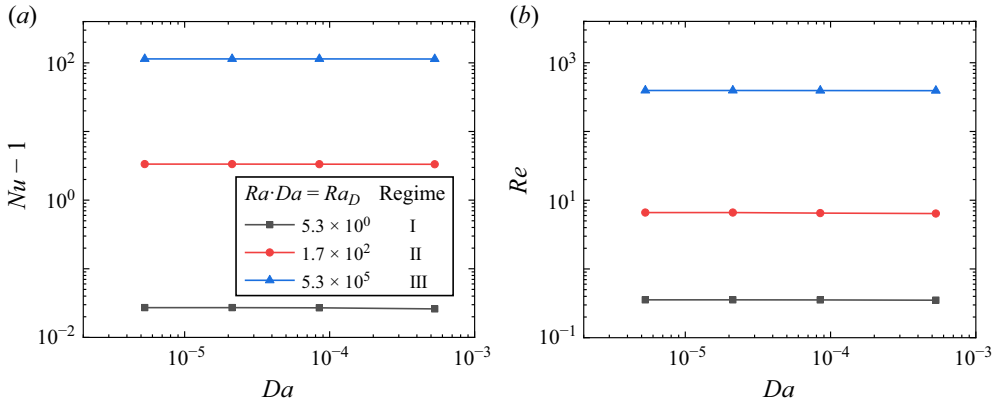


Figure 6. Dependence of (*a*) *Nu* and (*b*) *Re* on *Da* at $\phi = 0.69$. $N_r = 4, 10, 20, 40$, corresponding to $Da = K/H^2 = 5.3 \times 10^{-4}, 8.5 \times 10^{-5}, 2.1 \times 10^{-5}, 5.3 \times 10^{-6}$, respectively. Panels (*a*) and (*b*) share the same legend.

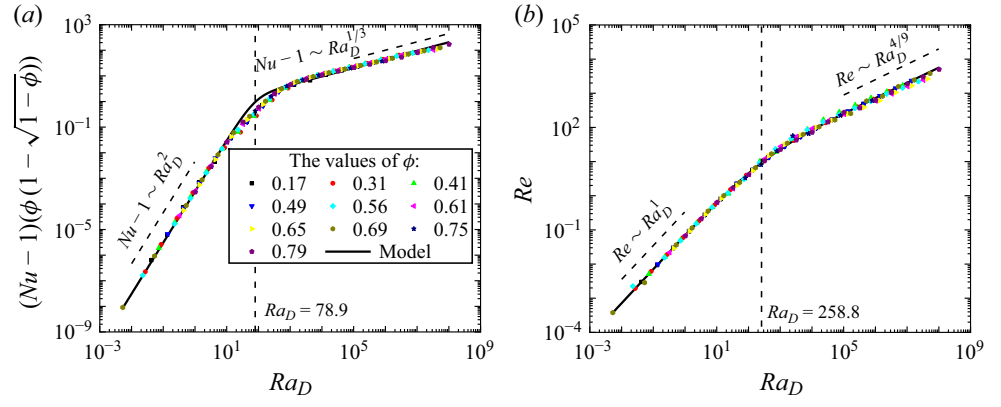


Figure 7. The relationships across a broad range of porosities. Panels show (*a*) $Nu - 1 \sim Ra_D$; (*b*) $Re \sim Ra_D$. Panels (*a*) and (*b*) share the same legend.

be approximated as a constant value. Consequently, bridge functions are proposed as illustrated below (Rao & Zhang 2025*a*,*b*)

$$Nu - 1 = a_1 Ra_D^{1/3}\left(1 + \left(Ra_D/Ra_D^{c1}\right)^{-5/3}\right)^{-1}\left(\phi\left(1 - \sqrt{1-\phi}\right)\right)^{-1}, \tag{3.11a}$$

$$Re = a_2 Ra_D^{4/9}\left(1 + \left(Ra_D/Ra_D^{c2}\right)^{-5/9}\right)^{-1}, \tag{3.11b}$$

where the prefactors a_1, a_2 and transitional values Ra_D^{c1}, Ra_D^{c2} are determined by fitting DNS results for $\phi = 0.69$ and equal (0.44, 1.57, 78.9, 258.8) respectively. Subsequently, the unified scaling models are validated against additional DNS results across various porosities.

Our analysis reveals that *Nu* and *Re* are independent of *Da* by conducting DNS cases, as well as being demonstrated in the unified scaling models. Various *Da* values are achieved by altering the number N_r of porous matrices, while maintaining a constant ϕ, as shown in (2.2) and figure 6. The results indicate that both *Nu* and *Re* remain nearly constant at each Ra_D, thereby confirming the independence of *Nu* and *Re* from *Da*. However, it is crucial to acknowledge that substantial errors may occur if *Da* continues to increase.

https://doi.org/10.1017/jfm.2025.11108 Published online by Cambridge University Press

The unified scaling models are validated against DNS results, as illustrated in figure 7. The results demonstrate a strong alignment between the model results and the DNS results in both the steady and turbulent regimes across a range of porosities. Notably, the scaling exponents ($\gamma_1 = 1/3$, $\gamma_2 = 4/9$) in regime III conform to GL theory (Grossmann & Lohse 2000; Ahlers *et al.* 2009; Liu *et al.* 2020), indicating the similarity between the present system and classical/porous-medium RBC. The critical Ra_D value for Nu is approximately 78.9, which closely corresponds with the theoretical critical Ra_D of 98.3 and the experimental value of 66.2 reported in the research (Kwok & Chen 1987). In contrast, the critical value for Re is approximately 258.8, which exceeds the critical Ra_D value for Nu. It is likely that Nu is significantly influenced by the factor Ra_D that causes it to transition to regime II earlier. Despite the minor discrepancies observed in regime II, the unified scaling models demonstrate universal applicability.

It is worth noting that the unified models presented in (3.11) do not imply that Da and ϕ have no influence on the scaling laws of Nu and Re. The effect of Da is partially represented in the term $Ra_D = Ra \cdot Da$. The influences of ϕ are also reflected in the permeability as described in (3.1*a*), and this dependence is embedded in the definition of $Ra_D = g\beta\Delta K H/(\nu\alpha)$. Furthermore, (3.11*a*) retains the term $(\phi(1-\sqrt{1-\phi}))^{-1}$, which also affects the determination of Nu. When ϕ approaches 1, the scaling law exponents of $Nu - 1 \sim Ra_D^{\gamma_1} Pr^{\eta_1}$ and $Re \sim Ra_D^{\gamma_2} Pr^{\eta_2}$ align with the GL theory and pure vertical natural convection with $\phi = 1$.

4. Conclusion

We have investigated vertical natural convection in a two-dimensional cavity filled with porous media over a broad range of Rayleigh–Darcy number Ra_D, porosity ϕ and Darcy number Da. Our findings reveal three major regimes characterised by the angle θ of the isothermal layer and flow states. Consequently, we theoretically derive distinct scaling laws for $Nu - 1 \sim Ra_D^{\gamma_1} Pr^{\eta_1}$ and $Re \sim Ra_D^{\gamma_2} Pr^{\eta_2}$. Regime I is dominated by Stokes flow and thermal conduction. We observe $\theta \approx \pi/2$ and derive $(\gamma_1, \gamma_2, \eta_1, \eta_2) = (2, 1, 0, -1)$ based on perturbation analysis. Regime III is characterised by turbulent flow and thermal convection with clear kinetic and thermal boundary layers. We observe $\theta \approx 0$ and derive $(\gamma_1, \gamma_2, \eta_1, \eta_2) = (1/3, 4/9, 0, -2/3)$, which aligns with GL theory. Regime II represents a transitional flow state, with corresponding parameters that fall between those of regimes I and III. The scaling laws are well validated by DNS results. Furthermore, we have established unified scaling models for $Nu - 1 \sim Ra_D$ and $Re \sim Ra_D$ at $Pr = 1$, effectively integrating three major regimes, and these remain accurate across a broad spectrum of Ra_D and ϕ. Our findings indicate that both Nu and Re are independent of Da when Da is sufficiently small. The unified scaling models are instrumental in predicting Nu and Re values based on the governing parameter Ra_D, thereby offering significant benefits to thermal convection and solutal convection.

In this study, we primarily focus on vertical natural convection in regular porous media. Future research will aim to extend this study to irregular porous media, particularly investigating the effects of the random distance between the left/right walls and the nearest porous matrix on the kinetic and thermal boundary layers. Notably, in regime III, the minimum pore scale may influence pore-scale turbulence, potentially altering the corresponding scaling exponents compared with those observed in regular porous media.

Funding. This research was supported by Zhejiang Provincial Natural Science Foundation of China (Grant No. LQN25E060006) and National Natural Science Foundation of China (Grant No. 12302284).

https://doi.org/10.1017/jfm.2025.11108 Published online by Cambridge University Press

Declaration of interests. The authors report no conflict of interest.

Appendix A. The global kinetic and thermal dissipation rates in porous-medium vertical natural convection

The global kinetic dissipation rate is equal to the global buoyancy work rate. The thermal dissipation rate can be expressed using Nu in a manner similar to classical RBC, but with $\tilde{\alpha}_0$ instead of α. Therefore, ε_u and ε_T can be expressed as

$$\begin{aligned}\varepsilon_u &= \nu\langle \boldsymbol{\nabla}\cdot(\boldsymbol{\nabla}\boldsymbol{u}\cdot\boldsymbol{u}) - \boldsymbol{u}\cdot\nabla^2\boldsymbol{u}\rangle_V = -\langle \boldsymbol{u}\cdot(\boldsymbol{u}\cdot\boldsymbol{\nabla}\boldsymbol{u} + \boldsymbol{g}\beta(T-T_0) + \rho^{-1}\boldsymbol{\nabla}p)\rangle_V \\ &= -\langle \boldsymbol{\nabla}\cdot(\boldsymbol{u}|\boldsymbol{u}|^2/2) - u_2 g\beta T + \rho^{-1}\boldsymbol{\nabla}\cdot(\boldsymbol{u}p)\rangle_V = g\beta\langle u_2 T\rangle_V, \end{aligned} \tag{A1}$$

$$\begin{aligned}\varepsilon_T &= \alpha\langle \boldsymbol{\nabla}\cdot(T\boldsymbol{\nabla}T) - T\nabla^2 T\rangle_V = \alpha\langle \boldsymbol{\nabla}\cdot(T\boldsymbol{\nabla}T) - (2\alpha)^{-1}\boldsymbol{\nabla}\cdot(\boldsymbol{u}T^2)\rangle_V \\ &= \alpha H^{-2}\oint_{\partial V_f} T\boldsymbol{\nabla}T\cdot\boldsymbol{n}\,\mathrm{d}S = \tilde{\alpha}_0\Delta^2 H^{-2}Nu, \end{aligned} \tag{A2}$$

where V_f denotes fluid phase and $\boldsymbol{n}$ denotes unit vector pointing from the fluid to solid at their interfaces. Regarding $\nabla^2 T_{Ra=0} = 0$ and $\delta T|_{x_1=\pm H/2} = 0$, ε_T can be further derived

$$\begin{aligned}\varepsilon_T &= \alpha\langle(\boldsymbol{\nabla}T_{Ra=0})^2 + (\boldsymbol{\nabla}\delta T)^2 + 2\boldsymbol{\nabla}T_{Ra=0}\cdot\boldsymbol{\nabla}\delta T\rangle_V \\ &= \tilde{\alpha}_0\Delta^2 H^{-2}Nu_{Ra=0} + \alpha\langle(\boldsymbol{\nabla}\delta T)^2\rangle_V + 2\alpha\langle\boldsymbol{\nabla}\cdot(\delta T\boldsymbol{\nabla}T_{Ra=0}) - \delta T\nabla^2 T_{Ra=0}\rangle_V \\ &= \tilde{\alpha}_0\Delta^2 H^{-2} + \alpha\langle(\boldsymbol{\nabla}\delta T)^2\rangle_V + 2\alpha H^{-2}\oint_{\partial V_f}\delta T\boldsymbol{\nabla}T_{Ra=0}\cdot\mathrm{d}\boldsymbol{S} \\ &= \tilde{\alpha}_0\Delta^2 H^{-2} + \alpha\langle(\boldsymbol{\nabla}\delta T)^2\rangle_V. \end{aligned} \tag{A3}$$

References

Ahlers, G., Grossmann, S. & Lohse, D. 2009 Heat transfer and large scale dynamics in turbulent Rayleigh–Bénard convection. *Rev. Mod. Phys.* **81** (2), 503–537.

Bodenschatz, E., Pesch, W. & Ahlers, G. 2000 Recent developments in Rayleigh–Bénard convection. *Annu. Rev. Fluid Mech.* **32** (1), 709–778.

De Paoli, M. 2023 Convective mixing in porous media: a review of Darcy, pore-scale and Hele-Shaw studies. *Eur. Phys. J. E* **46** (12), 129.

Ecke, R.E. & Shishkina, O. 2023 Turbulent rotating Rayleigh–Bénard convection. *Annu. Rev. Fluid Mech.* **55** (1), 603–638.

Grossmann, S. & Lohse, D. 2000 Scaling in thermal convection: a unifying theory. *J. Fluid Mech.* **407**, 27–56.

Hu, C. & Yang, Y. 2024 Double-diffusive convection with gravitationally unstable temperature and concentration gradients in homogeneous and heterogeneous porous media. *J. Fluid Mech.* **999**, A62.

Kwok, L.P. & Chen, C.F. 1987 Stability of thermal convection in a vertical porous layer. *J. Heat Transfer* **109** (4), 889–893.

Lappa, M. 2009 *Thermal Convection: Patterns, Evolution and Stability*. John Wiley Sons.

Li, J., Yang, Y. & Sun, C. 2024 From darcy flow to convective flow: pore-scale study of density-driven currents in porous media. arXiv preprint arXiv: 2409.19652.

Liu, S., Jiang, L., Chong, K.L., Zhu, X., Wan, Z.H., Verzicco, R., Stevens, R.J., Lohse, D. & Sun, C. 2020 From Rayleigh–Bénard convection to porous-media convection: how porosity affects heat transfer and flow structure. *J. Fluid Mech.* **895**, A18.

Liu, S., Jiang, L., Wang, C. & Sun, C. 2021 Lagrangian dynamics and heat transfer in porous-media convection. *J. Fluid Mech.* **917**, A32.

Lohse, D. & Shishkina, O. 2024 Ultimate Rayleigh–Bénard turbulence. *Rev. Mod. Phys.* **96** (3), 035001.

Lohse, D. & Xia, K.Q. 2010 Small-scale properties of turbulent Rayleigh–Bénard convection. *Annu. Rev. Fluid Mech.* **42** (1), 335–364.

Ng, C.S., Ooi, A., Lohse, D. & Chung, D. 2015 Vertical natural convection: application of the unifying theory of thermal convection. *J. Fluid Mech.* **764**, 349–361.

https://doi.org/10.1017/jfm.2025.11108 Published online by Cambridge University Press

NG, C.S., SPANDAN, V., VERZICCO, R. & LOHSE, D. 2020 Non-monotonic transport mechanisms in vertical natural convection with dispersed light droplets. *J. Fluid Mech.* **900**, A34.

NIELD, D.A. & BEJAN, A. 2006 *Convection in Porous Media*. Springer.

ODENTHAL, C., STEINMANN, W.D., ECK, M. & LAING, D. 2014 The cellflux storage concept for cost reduction in parabolic trough solar thermal power plants. *Energy Procedia* **46**, 142–151.

PIROZZOLI, S., DE PAOLI, M., ZONTA, F. & SOLDATI, A. 2021 Towards the ultimate regime in Rayleigh–Darcy convection. *J. Fluid Mech.* **911**, R4.

RAO, F. 2022 Direct numerical simulation and macroscopic modeling of turbulent flows in porous media. Thesis, Universität Bremen, Germany.

RAO, F. & JIN, Y. 2022 Possibility for survival of macroscopic turbulence in porous media with high porosity. *J. Fluid Mech.* **937**, A17.

RAO, F., KUZNETSOV, A.V. & JIN, Y. 2020 Numerical modeling of momentum dispersion in porous media based on the pore scale prevalence hypothesis. *Trans. Porous Med.* **133** (2), 271–292.

RAO, F. & ZHANG, S. 2025*a* Coupled modelling of turbulent forced thermal convection in anisotropic porous media. *J. Fluid Mech.* **1017**, A31.

RAO, F. & ZHANG, S. 2025*b* Heat-fluid-solid coupling model for turbulent forced convection within porous media. *Phys. Rev. Fluids* **10** (6), 064502.

RAO, F. & ZHANG, S. 2025*c* The in-depth analysis and validation of momentum dispersion modeling based on direct numerical simulation. *Phys. Fluids* **37** (1), 015142.

REBHI, R., MENNI, Y., LORENZINI, G. & AHMAD, H. 2022 Forced-convection heat transfer in solar collectors and heat exchangers: a review. *J. Adv. Res. Appl. Sci. Engng Technol.* **26** (3), 1–15.

SHISHKINA, O. 2016 Momentum and heat transport scalings in laminar vertical convection. *Phys. Rev. E* **93** (5), 051102.

TRIAS, F.X., GOROBETS, A., SORIA, M. & OLIVA, A. 2010 Direct numerical simulation of a differentially heated cavity of aspect ratio 4 with Rayleigh numbers up to 1011–part I: numerical methods and time-averaged flow. *Intl J. Heat Mass Transfer* **53** (4), 665–673.

TRIAS, F.X., SORIA, M., OLIVA, A. & PÉREZ-SEGARRA, C.D. 2007 Direct numerical simulations of two- and three-dimensional turbulent natural convection flows in a differentially heated cavity of aspect ratio 4. *J. Fluid Mech.* **586**, 259–293.

WANG, Q., LIU, H.R., VERZICCO, R., SHISHKINA, O. & LOHSE, D. 2021 Regime transitions in thermally driven high-Rayleigh number vertical convection. *J. Fluid Mech.* **917**, A6.

WANG, Q., XIA, S.N., YAN, R., SUN, D.J. & WAN, Z.H. 2019 Non-Oberbeck–Boussinesq effects due to large temperature differences in a differentially heated square cavity filled with air. *Intl J. Heat Mass Transfer* **128**, 479–491.

ZHANG, S., XIA, Z., ZHOU, Q. & CHEN, S. 2020 Controlling flow reversal in two-dimensional Rayleigh–Bénard convection. *J. Fluid Mech.* **891**, R4.

ZHU, X., FU, Y. & DE PAOLI, M. 2024 Transport scaling in porous media convection. *J. Fluid Mech.* **991**, A4.

https://doi.org/10.1017/jfm.2025.11108 Published online by Cambridge University Press